Single-electron gap in the spectrum of twisted bilayer graphene

A. V. Rozhkov, A. O. Sboychakov, A. L. Rakhmanov, and Franco Nori

Phys. Rev. B **95**, 045119 — Published 13 January 2017

DOI: 10.1103/PhysRevB.95.045119

Single-electron gap in the spectrum of twisted bilayer graphene

A.V. Rozhkov,[1,2,3] A.O. Sboychakov,[1,2] A.L. Rakhmanov,[1,2,3,4] and Franco Nori[1,5]

[1]*CEMS, RIKEN, Wako-shi, Saitama, 351-0198, Japan*
[2]*Institute for Theoretical and Applied Electrodynamics, Russian Academy of Sciences, 125412 Moscow, Russia*
[3]*Moscow Institute of Physics and Technology, Dolgoprudny, Moscow Region, 141700 Russia*
[4]*All-Russia Research Institute of Automatics, Moscow, 127055 Russia*
[5]*Department of Physics, University of Michigan, Ann Arbor, MI 48109-1040, USA*

We investigate the gap in the single-electron spectrum of twisted bilayer graphene. In a perfect infinite lattice of a twisted bilayer, the gap varies exponentially in response to weak changes of the twist angle. Such a large sensitivity makes theoretical predictions of the gap nearly impossible, since experimentally the twist angle is always known with finite accuracy. To address this issue, we numerically study finite clusters of twisted bilayer graphene. For finite systems, changing the twist angle causes a gradual crossover between gapless and gapped regimes. The crossover occurs when the finite-size quantization energy becomes comparable to the matrix elements responsible for the generation of the gap. We further argue that disorder scattering can induce similar crossover, in which the mean-free path plays the same role as the system size for the finite clusters. It is demonstrated that, to observe the gap experimentally, it is necessary to have a sample of suitable purity, and to possess the ability to tune the twist angle accurately.

PACS numbers: 73.22.Pr, 73.21.Ac

I. INTRODUCTION

Recent experimental studies (scanning tunneling microscopy, STM[1–4], Raman spectroscopy[5,6], angular resolved photoemission spectroscopy[7,8]) revealed that, in many cases, the structure of bilayer graphene samples is far from the ideal AB stacking. Instead, it is characterized by a non-zero twist angle θ between graphene layers. The electronic structure of twisted bilayer graphene (tBLG) is very rich, demonstrating a Dirac spectrum with a θ-dependent Fermi velocity[1,5], low-energy van Hove singularities[3,4], complex Fermi surface[9,10], and other peculiar features[12,13]. An important characteristic of its electronic structure is the single-electron gap. For twisted bilayer samples, the existence of the gap was demonstrated in several experiments[8,14]. This paper theoretically studies the gap (previous efforts on this issue are discussed in the recent review paper in Ref. 15).

If one is interested in the theoretical description of the tBLG, a useful starting point is to consider 'commensurate' values of θ for which the tBLG lattice forms commensurate superstructures. When the size of the supercell is not too large, the electronic properties can be studied numerically[9–11,17–25]. Besides computational approaches, several semi-analytic theories for low-energy electrons were developed[26–32]. Studying the commensurate angles, it is possible to calculate, for example, the dependence on θ of the Fermi velocity[27–29] $v_{\rm F}$ and the density of states[9]. Unfortunately, these approaches cannot be directly applied for the calculation of the gap. It was demonstrated in Ref. 9 that the gap Δ evaluated at the commensurate angles is not a smooth function of θ. Instead, it varies exponentially even for small changes of the twist angle. Clearly, such a large sensitivity implies that considering the commensurate angles is not sufficient for a consistent theory of how the gap is generated.

A possible way to remedy this situation was proposed in Ref. 9. It was pointed out that the sharp jumps of Δ were associated with the fact that the size of the supercell may change drastically for very small variations of θ. Therefore, the extreme sensitivity of Δ to the twist angle is possible only in a perfect infinite lattice of tBLG, where a superstructure with arbitrary large supercell can exist. Of course, any real sample has a finite linear size L. Furthermore, a realistic electron propagation is characterized by a finite mean free path $l_{\rm m}$ due to electron scattering on defects, such as impurities, "wrinkles" (as an example, below we will evaluate $l_{\rm m}$ for a particular case of a disordered ensemble of one-dimensional "wrinkles"), etc. The smallest among the length scales L and $l_{\rm m}$ would introduce a "cutoff", which disallows the superstructures with large supercells, and makes the jumps of Δ impossible[9].

The latter reasoning motivates us to investigate the formation of the gap in a tBLG sample of finite size. For tBLG clusters of various twist angles and linear sizes, we numerically determine the matrix elements, which couple different Dirac cones. By construction, the calculated matrix elements are smooth functions of θ. Since these matrix elements are small in comparison to the graphene band-width, many publications often dismiss them. Yet, they are important at low energies, causing qualitative changes to the electron spectrum: in the ideal infinite tBLG lattice they either open the gap, or induce a so-called "band splitting". In a finite-size sample, or in a sample with finite quasiparticle scattering, these cone-coupling matrix elements require a subtler interpretation: a gap cannot be observed, unless the corresponding matrix element exceeds both the dimensional quantization gap, and quasiparticle scattering frequency. We will demonstrate that this condition is satisfied only when θ is close to a commensurate angle with small supercell size. As the detuning from the "good" angle increases, the gap-generating matrix elements quickly (exponentially) decay, and the gap is washed away by the external scattering.

The paper is organized as follows. Section II summarizes

the geometry of the tBLG lattice. In Sec. III we discuss the general theoretical background of the problem considered. The scattering on the linear defects ("wrinkles"), which is a very effective mechanism limiting the coherent propagation of the electrons in graphene, is studied in Sec. IV. The numerical results for the finite-size samples are presented in Sec. V. The discussion and conclusions are given in Sec. VI. Additional details of the calculation of the matrix elements are presented in the Appendix.

II. GEOMETRY OF TWISTED BILAYER LATTICE

In this section, for reader's convenience, we provide basic information about the geometry of the twisted bilayer lattice. This will allow to introduce equations and notation which will be used later throughout this paper. The presentation here follows Refs. 9,15. A more general and comprehensive consideration of the slightly mismatched overlayers is done in Ref. 16.

A bilayer consists of two layers, one lying over the other. We will assume that the layers are perfectly flat, and separated by the distance $d = 3.35\,\text{Å}$ from each other. In a real tBLG sample the layers are not purely two-dimensional. The interlayer distance varies[3] depending on the local arrangement of the atoms. However, the interlayer corrugation is quite small ($\sim 0.1\,\text{Å}$), and our approximation is well-justified.

Each graphene layer consists of two sublattices, $A1$ and $B1$ in the layer 1 (bottom layer, see Fig. 1a), and $A2$, $B2$ in the layer 2 (top layer). In the layer 1 the positions of the carbon atoms are given by the equations

$$\mathbf{r}_{\mathbf{n}}^{1A} \equiv \mathbf{r}_{\mathbf{n}} = n\mathbf{a}_1 + m\mathbf{a}_2\,,\ \mathbf{r}_{\mathbf{n}}^{1B} = \mathbf{r}_{\mathbf{n}} + \boldsymbol{\delta}_1\,, \tag{1}$$

$$\boldsymbol{\delta}_1 = \frac{1}{3}(\mathbf{a}_1 + \mathbf{a}_2) = a(1/\sqrt{3},\,0)\,, \tag{2}$$

where $\mathbf{n} = (n, m)$ is a vector with integer-valued components n and m, the vector $\boldsymbol{\delta}_1$ points to a nearest-neighbor site on the honeycomb lattice, and $\mathbf{a}_{1,2}$ are primitive vectors of the lattice

$$\mathbf{a}_1 = \frac{a}{2}(\sqrt{3},\,-1), \qquad \mathbf{a}_2 = \frac{a}{2}(\sqrt{3},\,1), \tag{3}$$

with the lattice parameter $a = 2.46\,\text{Å}$. We will also use the length of the in-plane carbon-carbon bond $a_0 = a/\sqrt{3} = 1.42\,\text{Å}$.

When $\theta = 0$, the system is a perfect AB bilayer. Let us consider the situation when the layer 2 is rotated with respect to layer 1 by the angle θ around the axis connecting the atoms $A1$ and $B2$ with $\mathbf{n} = 0$ (see Fig. 1). The atoms of the rotated layer, thus, have the positions

$$\mathbf{r}_{\mathbf{n}}^{2B} \equiv \mathbf{r}'_{\mathbf{n}} = n\mathbf{a}'_1 + m\mathbf{a}'_2\,,\ \mathbf{r}_{\mathbf{n}}^{2A} = \mathbf{r}'_{\mathbf{n}} - \boldsymbol{\delta}'_1\,, \tag{4}$$

where

$$\mathbf{a}'_{1,2} = \mathbf{a}_{1,2}\left(\cos\theta \mp \frac{\sin\theta}{\sqrt{3}}\right) \pm \mathbf{a}_{2,1}\frac{2\sin\theta}{\sqrt{3}}\,, \tag{5}$$

$$\boldsymbol{\delta}'_1 = \frac{a}{\sqrt{3}}(\cos\theta,\,\sin\theta)\,. \tag{6}$$

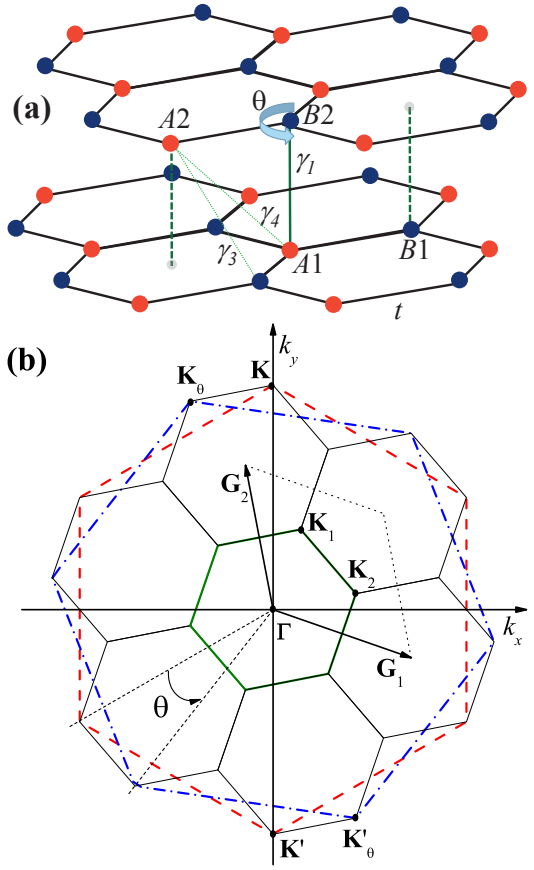

FIG. 1: (a) Starting from a perfect AB-bilayer graphene, a twisted graphene bilayer is obtained by rotating the top layer by the angle θ (shown by the blue rotating arrow). The rotation is performed around the axis connecting sites $A1$ and $B2$; the quantity t is the in-plane nearest-neighbor hopping, and $\gamma_{1,3,4}$, are out-of-plane hopping amplitudes of the AB-stacked bilayer. These γs are used to fix the fitting parameters of the function $t_\perp(\mathbf{r};\mathbf{r}')$ (see the text). In this paper we use $\gamma_1 = 0.4$ eV, $\gamma_3 = 0.254$ eV, and $\gamma_4 = 0.051$ eV, which are all substantially smaller than the in-plane hopping amplitude $t = 2.8$ eV. (b) Reciprocal space structure for $\theta = 21.787^\circ$ ($m_0 = 1$, $r = 1$). The large hexagons show the Brillouin zones of individual layers: the red dashed (the blue dot-dashed) hexagon corresponds to the bottom (top) layer. The green thick solid hexagon represents the first Brillouin zone of the bilayer. The next several Brillouin zones of the tBLG are shown by black thin solid hexagons. The Dirac point $\mathbf{K}'$ ($\mathbf{K}'_\theta$) is equivalent to the point $\mathbf{K}_\theta$ ($\mathbf{K}$) if $r \neq 3n$. When $r = 3n$, $\mathbf{K}_\theta \sim \mathbf{K}$ and $\mathbf{K}'_\theta \sim \mathbf{K}'$ (see the text). The tBLG Dirac points $\mathbf{K}_{1,2}$ are doubly degenerate: each of them is equivalent to one of two Dirac points of each graphene layer. For the particular case of the $(1,1)$ superstructure, $\mathbf{K}_1 \sim \mathbf{K} \sim \mathbf{K}'_\theta$, and $\mathbf{K}_2 \sim \mathbf{K}' \sim \mathbf{K}_\theta$.

The structure of the tBLG is commensurate if[19,26–28]

$$\cos\theta = \frac{3m_0^2 + 3m_0 r + r^2/2}{3m_0^2 + 3m_0 r + r^2}\,, \tag{7}$$

where m_0 and r are coprime positive integers. For these an-

gles the superlattice vectors $\mathbf{R}_{1,2}$ are:

$$\begin{cases} \mathbf{R}_1 &= m_0\mathbf{a}_1 + (m_0+r)\mathbf{a}_2 \\ \mathbf{R}_2 &= -(m_0+r)\mathbf{a}_1 + (2m_0+r)\mathbf{a}_2 \end{cases} \quad (r \neq 3n,\ n \in \mathbb{N}), \tag{8}$$

or

$$\begin{cases} \mathbf{R}_1 &= (m_0+n)\mathbf{a}_1 + n\mathbf{a}_2 \\ \mathbf{R}_2 &= -n\mathbf{a}_1 + (m_0+2n)\mathbf{a}_2 \end{cases} \quad (r = 3n,\ n \in \mathbb{N}). \tag{9}$$

An important property of the superlattice is the number of sites in a supercell. It equals to

$$N(m_0, r) = \begin{cases} 4(3m_0^2 + 3m_0 r + r^2), \text{ if } r \neq 3n\,, \\ 4(m_0^2 + m_0 r + r^2/3), \text{ if } r = 3n\,. \end{cases} \tag{10}$$

The linear size of the superlattice cell is $L_{\rm sc} \equiv |\mathbf{R}_{1,2}| = a\sqrt{N}/2$.

The primitive vectors of the reciprocal superlattice can be written as

$$\begin{aligned} \mathbf{G}_1 &= \frac{(2m_0+r)\mathbf{b}_1 + (m_0+r)\mathbf{b}_2}{3m_0^2 + 3m_0 r + r^2}\,, \\ \mathbf{G}_2 &= \frac{-(m_0+r)\mathbf{b}_1 + m_0\mathbf{b}_2}{3m_0^2 + 3m_0 r + r^2}, \quad \text{if } r \neq 3n, \end{aligned} \tag{11}$$

or

$$\begin{aligned} \mathbf{G}_1 &= \frac{(m_0+2n)\mathbf{b}_1 + n\mathbf{b}_2}{m_0^2 + m_0 r + r^2/3}\,, \\ \mathbf{G}_2 &= \frac{-n\mathbf{b}_1 + (m_0+n)\mathbf{b}_2}{m_0^2 + m_0 r + r^2/3}, \quad \text{if } r = 3n, \end{aligned} \tag{12}$$

where $\mathbf{b}_{1,2}$ are the reciprocal lattice vectors of the single layer graphene

$$\mathbf{b}_1 = \frac{2\pi}{\sqrt{3}a}(1, -\sqrt{3})\,, \qquad \mathbf{b}_2 = \frac{2\pi}{\sqrt{3}a}(1, \sqrt{3})\,. \tag{13}$$

The first Brillouin zone of the superlattice has the shape of a hexagon with side $|\mathbf{G}_2 - \mathbf{G}_1|/3$. In the particular case $r = 1$, this side is equal to $\Delta K = |\mathbf{K}_\theta - \mathbf{K}|$, where

$$\mathbf{K} = \frac{4\pi}{3a}(0,\, 1) \quad \text{and} \quad \mathbf{K}_\theta = \frac{4\pi}{3a}(-\sin\theta,\, \cos\theta) \tag{14}$$

are the Dirac points of the bottom and top layers, respectively. The electron states near the points $\mathbf{K}$ and $\mathbf{K}_\theta$ have identical chiralities. The points of opposite chirality are located at $\mathbf{K}' = -\mathbf{K}$ and $\mathbf{K}'_\theta = -\mathbf{K}_\theta$. In the Brillouin zone of the superstructure, the Dirac points coordinates are given by the following expressions

$$\begin{aligned} \mathbf{K} &= -\mathbf{K}' = m_0\mathbf{G}_2 + \frac{r}{3}\left(\mathbf{G}_1 + 2\mathbf{G}_2\right), \\ \mathbf{K}_\theta &= -\mathbf{K}'_\theta = m_0\mathbf{G}_2 + \frac{r}{3}\left(\mathbf{G}_2 - \mathbf{G}_1\right), \end{aligned} \tag{15}$$

if $r \neq 3n$, or

$$\begin{aligned} \mathbf{K} &= -\mathbf{K}' = \frac{r}{3}\mathbf{G}_2 + \frac{m_0}{3}\left(\mathbf{G}_2 - \mathbf{G}_1\right), \\ \mathbf{K}_\theta &= -\mathbf{K}'_\theta = -\frac{r}{3}\mathbf{G}_1 + \frac{m_0}{3}\left(\mathbf{G}_2 - \mathbf{G}_1\right), \end{aligned} \tag{16}$$

if $r = 3n$.

One can check that, if $r \neq 3n$, point $\mathbf{K}'$ is equivalent to $\mathbf{K}_\theta$, and $\mathbf{K}$ is equivalent to $\mathbf{K}'_\theta$:

$$\mathbf{K}' \sim \mathbf{K}_\theta \quad \text{and} \quad \mathbf{K} \sim \mathbf{K}'_\theta \quad \text{for } r \neq 3n. \tag{17}$$

Indeed, for such a value of r, the difference $\mathbf{K}' - \mathbf{K}_\theta$ is a reciprocal vector of the superlattice. When $r = 3n$, the equivalency relations are different:

$$\mathbf{K} \sim \mathbf{K}_\theta \quad \text{and} \quad \mathbf{K}' \sim \mathbf{K}'_\theta \quad \text{for } r = 3n. \tag{18}$$

Thus, for any commensurate angle we have two doubly-degenerate non-equivalent Dirac points of the tBLG. It follows from Eqs. (15) and (16) that inside the reciprocal cell of the superlattice, the two non-equivalent tBLG Dirac points are located at

$$\mathbf{K}_1 = \frac{\mathbf{G}_1 + 2\mathbf{G}_2}{3}\,, \quad \mathbf{K}_2 = \frac{2\mathbf{G}_1 + \mathbf{G}_2}{3}\,. \tag{19}$$

Double degeneracy of these Dirac cones affects the electronic structure of the tBLG leading to the band splitting and band gap formation.

Besides $L_{\rm sc}$, the tBLG has another characteristic length scale. The rotation of one graphene layer with respect to another leads to the appearance of Moiré patterns, manifesting in STM experiments[1–4] as alternating bright and dark regions. The Moiré period $L_{\rm M}$ is defined as the distance between the centers of two neighboring bright (or dark) regions. It is related to the twist angle as

$$L_{\rm M} = \frac{a}{2\sin(\theta/2)}\,. \tag{20}$$

It is possible to establish that the superstructure coincides with the Moiré pattern when $r = 1$. For other superstructures, $L_{\rm sc}$ is greater than $L_{\rm M}$. The supercells of these structures contain r^2 (if $r \neq 3n$) or $r^2/3$ (if $r = 3n$) Moiré cells, and the arrangements of atoms inside these Moiré cells are slightly different from each other. This means, in particular, that the structures with $r > 1$ can be considered as almost periodic repetitions[28] of structures with $r = 1$. The Moiré pattern and the superstructure are two complementary concepts used to describe the tBLG.

The Moiré pattern depends smoothly on the twist angle, as demonstrated by Eq. (20), and can be easily detected experimentally. However, working with the Moiré theoretically may be challenging since the Moiré structure is strictly periodic for a very limited discrete set of angles. For a generic value of θ, different Moiré cells in the pattern may look alike, but they are not exactly identical.

The superstructure, which is a periodic lattice of supercells, does not suffer from this shortcoming. Unfortunately, it has its own deficiencies. Namely, the superstructure is defined for commensurate angles θ only. The period $L_{\rm sc}$ is not a smooth function of θ: two commensurate angles, θ and θ', $\theta \approx \theta'$, may correspond to two very dissimilar $L_{\rm sc}$. The existence of two length scales, $L_{\rm M}$ and $L_{\rm sc}$, in tBLG affects its electronic properties[19]. While some physical quantities (for example,

renormalized Fermi velocity) are insensitive to sharp variations of $L_{\rm sc}$ versus θ, others (for example, the gap) are not[9]. Consequently, Fermi velocity calculations at commensurate angles are sufficient for adequate theoretical description; yet, the situation with the gap is more delicate, as we will show below.

III. LOW-ENERGY EFFECTIVE MODEL

The opening of the gap can be heuristically deduced from the discussion of Sec. II. Indeed, the low-energy dispersion of the tBLG is characterized by four Dirac points, two from each layer. At commensurate angles the four points can be grouped into two equivalence classes, see Eq. (17) and (18). In other words, while in the original reciprocal space of two sheets of the single-layer graphene all four Dirac points have different coordinates, after folding to the first Brillouin zone of the superlattice the equivalent Dirac points end up in identical locations. The electron states near equivalent points may be connected by non-zero matrix elements of the interlayer tunneling operator $t_\perp$: in the presence of the superlattice such matrix elements are consistent with the quasimomentum conservation law. Although the absolute values of these matrix elements are small, the kinetic energy of electrons near the Dirac points is small as well. As a result, the interlayer tunneling qualitatively affects the low-energy spectrum.

To formalize this reasoning, a low-energy effective model is very useful. In the case of commensurate structures, we can write the low-energy Hamiltonian in a given corner of the Brillouin zone in the form

$$H^{\rm tBLG}_{\mathbf{k}} = \begin{pmatrix} H^{\rm D}_{\gamma\mathbf{k}}(0) & M \\ M^\dagger & H^{\rm D}_{\gamma'\mathbf{k}}(\theta) \end{pmatrix}. \qquad (21)$$

In this expression the (quasi)momentum $\mathbf{k}$ is measured from the superlattice Brillouin zone corner, while the single-layer Dirac Hamiltonian $H^{\rm D}_{\gamma\mathbf{k}}(\theta)$ for the rotation angle θ and cone chirality index $\gamma = \mathbf{K}, \mathbf{K}'$ equals

$$H^{\rm D}_{\gamma\mathbf{k}}(\theta) = v_{\rm F}\left(k_x\sigma_y^\theta \mp k_y\sigma_x^\theta\right). \qquad (22)$$

Here $v_{\rm F}$ is the Fermi velocity and $\sigma^\theta_{x,y} = e^{\frac{i\theta}{2}\sigma_z}\sigma_{x,y}e^{-\frac{i\theta}{2}\sigma_z}$ are the "rotated" Pauli matrices, and the sign in Eq. (22) depends on the chirality index γ. For structures $r \neq 3n$, the chirality indices in the Hamiltonian (21) are unequal $\gamma \neq \gamma'$. Otherwise, $\gamma = \gamma'$. The matrix elements $M_{\alpha\beta}$ of the 2×2 matrix M are given by the equation

$$M_{\alpha\beta} = \sum_{\mathbf{nm}} (\psi^{1\alpha}_\gamma(\mathbf{r}^{1\alpha}_\mathbf{n}))^*\ \psi^{2\beta}_{\gamma'}(\mathbf{r}^{2\beta}_\mathbf{m})\ t_\perp(\mathbf{r}^{1\alpha}_\mathbf{n}, \mathbf{r}^{2\beta}_\mathbf{m}). \qquad (23)$$

In this expression, the interlayer tunneling amplitude $t_\perp(\mathbf{r}^{1\alpha}_\mathbf{n}, \mathbf{r}^{2\beta}_\mathbf{m})$ depends on the location $\mathbf{r}^{1\alpha}_\mathbf{n}$ of an atom in layer 1, sublattice α, and the location $\mathbf{r}^{2\beta}_\mathbf{m}$ of an atom in layer 2, sublattice β, see Eqs. (1) and (4). The symbol $\psi^{i\alpha}_\gamma$ denotes a spinor component of the wave function in layer $i = 1, 2$, on the sublattice $\alpha = A, B$ with chirality γ. The wave function corresponds to the Dirac point: $\psi^{1\alpha}_\gamma(\mathbf{r}^{1\beta}_\mathbf{n})$ vanishes, if $\alpha \neq \beta$, and $\psi^{1\alpha}_\gamma(\mathbf{r}) \propto \exp(\pm i\mathbf{Kr})$, where the sign depends on γ. For layer 2 the wave function is derived from $\psi^{1\alpha}_\gamma(\mathbf{r}^{1\beta}_\mathbf{n})$ by suitable rotation of the atoms positions.

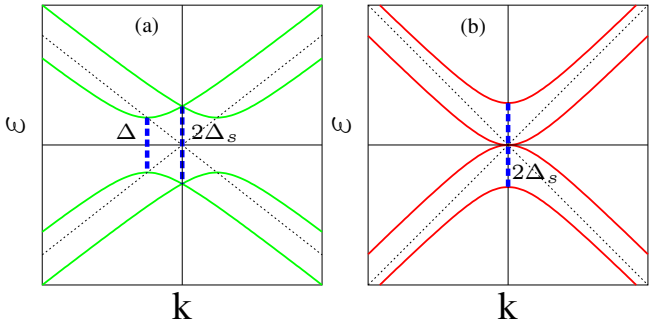

FIG. 2: Schematic structure of the low-energy dispersion of twisted bilayer graphene for $r \neq 3n$ [panel (a)] and $r = 3n$ structures [panel (b)]. Dotted lines represent two degenerate Dirac cones. When the matrix M is non-zero, this degeneracy is lifted. The resultant dispersion is shown by solid [green (a) and red (b)] lines. Vertical dashed lines mark the energy scales Δ and Δ_s. The $r = 3n$ structures have no gap, however, their density of states decreases below Δ_s. For $r \neq 3n$ structures, the spectral gap Δ and the scale $2\Delta_s$ are not identical. However, numerical evidence[9] suggests that the latter scales are of the same order.

Strictly speaking, the effective Hamiltonian (21) is applicable only for large twist angles, $15^\circ \lesssim \theta \lesssim 45^\circ$. For smaller angles (or for $\theta \gtrsim 45^\circ$), the interlayer matrix elements connecting the electron states with the same chirality γ but different momenta (constrained, of course, by the superlattice quasimomentum conservation law) become of importance[27,28]. Such coupling terms result in the downward renormalization of the Fermi velocity. We can take this renormalization into account by replacing $v_{\rm F}$ in Eq. (22) by the angle-dependent function $v^*_F(\theta)$.

We calculate the matrix elements of M numerically, both for infinite and finite samples, with different values of θ. For the latter case, the twist angle can be arbitrary, not necessarily commensurate. Calculating M we used the parametrization for the hopping amplitudes $t_\perp(\mathbf{r}^{1\alpha}_\mathbf{n}, \mathbf{r}^{2\beta}_\mathbf{m})$ proposed in Ref. 33. The same parametrization was used in our previous work Ref. 9. Details of the computational procedure are presented in Appendix A. Our numerical analysis, as well as arguments of Ref. 30, reveals that the matrix M is sensitive to whether the parameter r is a multiple of 3, or not. More precisely, the structure of the matrix M is the following:

$$M = \begin{pmatrix} 0 & me^{i\alpha} \\ me^{i\beta} & 0 \end{pmatrix}, \quad \text{when } r \neq 3n, \qquad (24)$$

or

$$M = \begin{pmatrix} 0 & 0 \\ me^{i\beta} & 0 \end{pmatrix}, \quad \text{when } r = 3n, \qquad (25)$$

where m, α, and β are real numbers.

The general structure of the Hamiltonian (21) coincides to that proposed in Ref. 30. The main difference lies in the parametrization of the interlayer hopping amplitudes used to

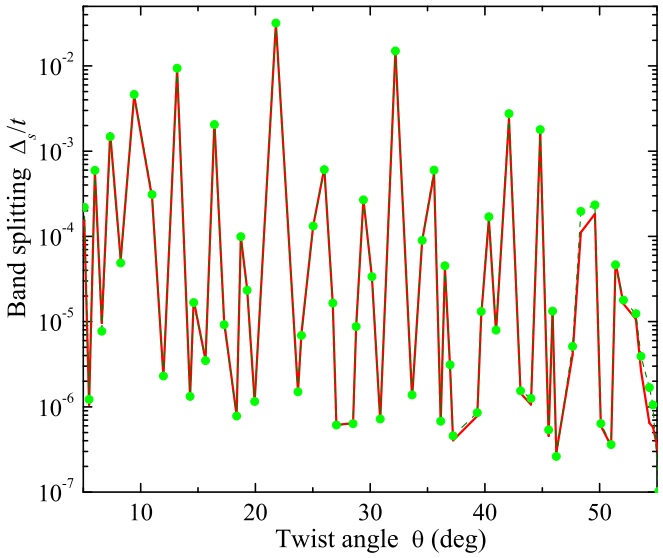

FIG. 3: Band splitting Δ_s for ideal superlattices with supercell sizes $N < 2000$. Circles (green) connected by the dashed (blue) line present the results of calculations using Eq. (23), while solid (red) line corresponds to the tight-binding calculations of Ref. 9. The data are shown for $r \neq 3n$ structures only. The sharp exponential jumps of Δ_s, which we observe in this figure, can exist only in the idealized infinite tBLG lattice.

calculate M. Our parametrization is able to correctly describe the limiting case of the AB bilayer ($\theta = 0$), as it is explained in Ref. 9.

The low-energy spectrum is found by diagonalizing the 4×4 matrix Eq. (21). It consists of four bands with dispersions $E_{\mathbf{k}}^{(s)}$ ($s = 1, 2, 3, 4$) given by

$$E_{\mathbf{k}}^{(1,2,3,4)} = \pm\sqrt{\Delta^2 + v_{\rm F}^2(|\mathbf{k}| \mp k_0)^2}\,, \quad \text{if } r \neq 3n, \quad (26)$$

or, for $r = 3n$,

$$E_{\mathbf{k}}^{(1,4)} = \mp\sqrt{\Delta_s^2 + v_{\rm F}^2\mathbf{k}^2}, \quad (27)$$

$$E_{\mathbf{k}}^{(2,3)} = \pm\left(\sqrt{\Delta_s^2 + v_{\rm F}^2\mathbf{k}^2} - \Delta_s\right), \quad (28)$$

where

$$\Delta_s = |m|, \quad \Delta = |m\cos[(\alpha-\beta)/2]|, \quad (29)$$

$$k_0 = m\sin[(\alpha-\beta)/2]. \quad (30)$$

The spectra (26) and (27) are schematically shown in Fig. 2. For structures with $r \neq 3n$ [see Fig. 2(a)], the tBLG is an insulator with a well-defined gap Δ. If $r = 3n$, the density of states $\rho(\varepsilon)$ is finite even at $\varepsilon = 0$. However, $\rho(\varepsilon)$ experiences a depression when $|\varepsilon| < \Delta_s = |m|$, see Fig. 2(b).

The energy scale Δ_s will be referred to as the band splitting. We measure here the value of Δ_s in units of the graphene's nearest-neighbor hopping amplitude t, which is related to the Fermi velocity as[15,34] $v_{\rm F} = 3ta_0/2$. Thus, according to the low-energy model (21), the band splitting Δ_s is simply a matrix element, whose calculation does not require diagonalization of any matrix. To check the validity of the model (21) itself we compare Δ_s with the results of the tight-binding calculations of the same quantity, performed in Ref. 9. The curves presented in Fig. 2 show a very good correlation between results given by two theoretical approaches even for small twist angles where the effective model (21) is not formally applicable. For structures with $r \neq 3n$, the value of $2\Delta_s$ is larger than the band gap by a factor of order unity[9]. Thus, the band splitting given by the modulus of the non-zero matrix elements in M is a computationally efficient quantity, which can be used to estimate the possible size of the single-electron gap. In this paper we will consider the band splitting as a measure of the low-energy spectrum rearrangement, induced by the interlayer tunneling.

Working with Δ_s instead of Δ reduces the computational complexity. However, the main issue remains: the elements in the matrix M, when calculated for an infinite superlattice, are not smooth functions of θ, as shown in Fig. 3. This problem disappears for finite tBLG samples: by construction [see Eq. (23)], the matrix elements become analytical functions of the twist angle. Physically, the finite linear size of the tBLG cluster may indeed correspond to finite dimensions of a mesoscopic system, or it may mimic a finite mean free path of an electron due to scattering by disorder, such as wrinkles and impurities.

Yet, we must remember that a non-zero m in a finite-size system does not immediately imply the existence of a non-zero gap. The gap could be observed experimentally only when m exceeds the dimensional quantization energy $\delta\varepsilon = v_{\rm F}/L$, or the disorder scattering rate $\Gamma \sim v_{\rm F}/l_{\rm m}$ in a sample with disorder. The requirement

$$\Delta_s(\theta) > \max(\delta\varepsilon, \Gamma) \quad (31)$$

places significant restrictions on the values of θ, for which the spectrum is gapped. As this condition is violated, the gap is washed away by external scattering by disorder or edges. This will be discussed in Section V.

IV. SCATTERING BY LINEAR DEFECTS

We argued in the previous section that disorder can destroy the spectral gap. In a tBLG there are several possible sources of electron scattering (electron-electron interaction, point-like neutral and charged impurities, "wrinkles", and others). Studying all of them is beyond the scope of this paper. In this section, we show that the (inherent for graphene systems) linear defects ("wrinkles") are very effective scatterers in the tBLG, giving rise to a finite mean-free-path $l_{\rm m}$ when $\varepsilon \to 0$. Our calculations are quite simple, but they allow us to demonstrate the emergence of the finite energy-independent mean free path in a disordered system of Dirac electrons.

Let us now consider "a wrinkle", a one-dimensional defect stretching along the y-axis. We model this defect by a potential $V(x, y) = v_{\rm F}\bar{V}\delta(x)$, where the dimensionless parameter

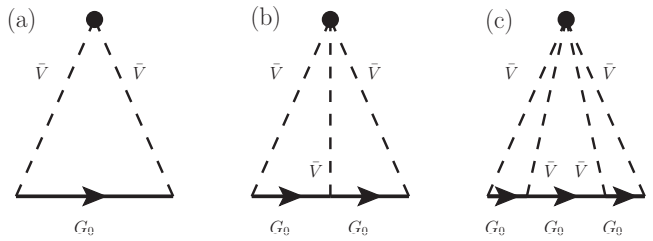

FIG. 4: Self-energy diagrams for scattering on a single defect. The defect is represented by a black circle, dashed lines labeled by $\bar{V}$ correspond to the defect potential. Solid lines with arrows are the electron propagator. Panel (a) shows the lowest-order contribution to the self-energy. It equals to $\bar{V}\hat{\sigma}_0 = O(\bar{V}^2)$ and corresponds to the Born approximation. The higher-order corrections are shown in panels (b) and (c).

$\bar{V}$ characterizes "the strength" of the defect. Neglecting interlayer hopping, the propagation of the low-energy electron in the graphene layer is described by the Hamiltonian Eq. (22). Within the Born approximation, the self-energy correction due to the wrinkle equals to $v_{\rm F}\bar{V}\hat{\sigma}_0/L_x$, where L_x is the linear dimension of the sample in the x direction. The quantity $\hat{\sigma}_0$ is proportional to the usual second-order impurity-scattering loop diagram [see panel (a) of Fig. 4]

$$\hat{\sigma}_0 = \frac{v_{\rm F}\bar{V}}{2\pi}\int dk_x\; G_0(\varepsilon,\mathbf{k})\,, \tag{32}$$

where the bare Green's function G_0 for the Hamiltonian Eq. (22) is equal to

$$G_0 = \frac{1}{(\varepsilon+i0)^2 - v_{\rm F}^2|\mathbf{k}|^2}\begin{pmatrix}\varepsilon & v_{\rm F}(k_x - ik_y)\\ v_{\rm F}(k_x+ik_y) & \varepsilon\end{pmatrix}.$$

The integral in Eq. (32) is easy to calculate

$$\hat{\sigma}_0 = -\frac{i\bar{V}}{2\sqrt{\varepsilon^2 - v_{\rm F}^2k_y^2}}\begin{pmatrix}\varepsilon & -iv_{\rm F}k_y\\ iv_{\rm F}k_y & \varepsilon\end{pmatrix}\operatorname{sgn}\varepsilon\,. \tag{33}$$

To obtain the full self-energy it is necessary to sum the self-energy diagrams to all orders of $\bar{V}$. The three lowest-order terms of this series are shown in Fig. 4. Since the n-th order diagram is proportional to $\hat{\sigma}_0^n$, the summation is performed trivially, and one derives

$$\hat{\Sigma}_0 = \frac{v_{\rm F}}{L_x}\frac{\bar{V}\hat{\sigma}_0}{1-\hat{\sigma}_0}\,. \tag{34}$$

This self-energy conserves the energy ε and momentum k_y. As for k_x, it is not conserved: upon scattering off the wrinkle, the momentum projection k_x can change arbitrarily with finite probability. For an ensemble of wrinkles we must average over the location of the wrinkle. This procedure restores the conservation of k_x, and the resultant self-energy becomes

$$\hat{\Sigma} = n_{\rm w}\frac{v_{\rm F}\bar{V}\hat{\sigma}_0}{1-\hat{\sigma}_0}\,, \tag{35}$$

where $n_{\rm w}$ is the concentration of the "wrinkles" (it has a dimension of the inverse length). The self-energy $\hat{\Sigma}$ is diagonal both in ε and in $\mathbf{k}$.

The averaging over the location of the wrinkle, which we performed to derive Eq. (35), must be supplemented by the averaging over the orientations of the wrinkles. After all, in a generic situation, an ensemble of wrinkles is likely to be fairly isotropic. To perform this averaging it is useful to notice that the matrix $\hat{\sigma}_0$ has two eigenvalues

$$\sigma^{\pm} = -\frac{i\bar{V}}{2\sqrt{\varepsilon^2 - v_{\rm F}^2k_y^2}}(\varepsilon \pm v_{\rm F}k_y)\operatorname{sgn}\varepsilon\,, \tag{36}$$

which correspond to the eigenvectors $(1,\pm i)/\sqrt{2}$. The matrix $\hat{\Sigma}$ will have the same eigenvectors. The eigenvalues of $\hat{\Sigma}$ can be found using Eqs. (35) and (36).

Since the eigenvectors of $\hat{\Sigma}$ are independent of both ε and k_y, we need to average the eigenvalues only. Further simplification can be obtained if we work on the mass surface. There one can write $v_{\rm F}k_y = \varepsilon\sin\phi$, where ϕ denotes the angle of incidence of the electron on the wrinkle. The eigenvalues of $\hat{\Sigma}$ on the mass surface are

$$\Sigma^{\pm}_{\rm m.s.} = -n_{\rm w}\frac{i\bar{V}^2(1\pm\sin\phi)}{2|\cos\phi| + i\bar{V}(1\pm\sin\phi)}\,. \tag{37}$$

The required integration over ϕ is well-defined for any nonzero $\bar{V}$. It is clear that after such an integration both eigenvalues become identical, and the averaged self-energy is proportional to the scalar matrix. In the limit of small $\bar{V}$ we obtain

$$\Sigma_{\rm m.s.} = -i\bar{V}^2 n_{\rm w}\int\limits_{-\pi/2}^{\pi/2}\frac{d\phi}{2\pi}\frac{\cos\phi}{\cos^2\phi + \bar{V}^2}\,, \tag{38}$$

which implies that the scattering rate is

$$\Gamma \propto n_{\rm w}\bar{V}^2\ln\bar{V}\,. \tag{39}$$

This relation for the scattering rate was derived under the assumption that the multiple-wrinkle scattering effects may be neglected. Thus, the localization cannot be described in the framework of the above procedure. The expression for Γ is energy-independent, and is valid at low energies. Unlike point-like impurities, whose scattering in graphene becomes weaker (for weak impurity potentials) as the quasiparticle energy lowers[35], the linear defects scatter well even at the Dirac point. Consequently, the electrons acquire a finite mean free path $l_{\rm m} \sim v_{\rm F}/\Gamma < \infty$. This limits the coherent propagation of the electron wave packet, and destroys weak interference effects due to superstructures with large supercell sizes.

V. GAP AND BAND SPLITTING FOR FINITE SAMPLES

Thus, the coherent propagation of an electron in a tBLG sample is always limited to some finite length scale. In the present study, to mimic this length we modeled a tBLG as a

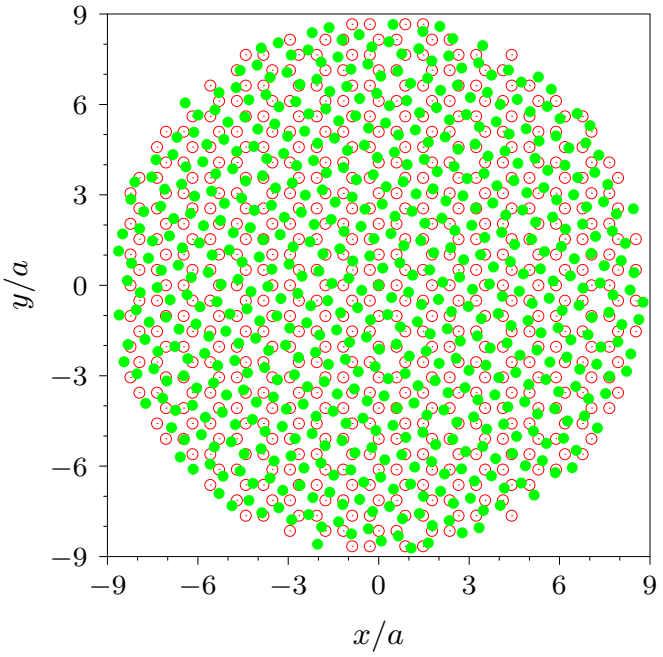

FIG. 5: Cluster of tBLG. Radius $R = 15a_0 = 5\sqrt{3}a$, with a rotation angle $\theta = 16.7^\circ$. The bottom layer is shown by open (red) circles, while the top (rotated) layer by filled (green) circles.

cluster of finite size, see Fig. 5. The cluster has circular shape, it consists of the sites of the tBLG lattice whose distance from the origin is less than the cluster radius R. For example, the cluster in Fig. 5 has $R = 15a_0 = 5\sqrt{3}a$.

As shown in Section III in the framework of the low-energy model (21), the band splitting Δ_s is equal to the modulus of the non-zero matrix element(s) of the matrix M, see Eq. (29). Likewise, the band gap Δ is proportional to $|m|$. We calculate these matrix elements numerically as prescribed by Eqs. (23), (24), and (25), for a range of R's and θ's (additional technical details can be found in the Appendix). The typical behavior of $|m|$ is shown in Fig. 6, where numerical data, in the window $14^\circ < \theta < 46^\circ$, is plotted for a cluster of radius $R/a_0 = 60$. Both $r \neq 3n$ and $r = 3n$ data are presented. The pronounced peaks in Fig. 6 occur at "good" angles corresponding to the superlattices with small supercells. Smaller peaks may be associated with some finite-size effects: these peaks sharply weaken when R is increased.

It is known[15] that for a $r \neq 3n$ structure, characterized by the twist angle θ, one can construct a conjugate $r = 3n$ structure with the angle

$$\theta' = 60^\circ - \theta\,, \tag{40}$$

such that both structures have the same supercell size. The data in Fig. 6 illustrates this relation: two strongest peaks are located at angles 21.7° and 38.2°, whose sum equals to 60°. The same is true for the pair of the second-strongest peaks at 27.8° and 32.2°.

The matrix element $|m|$, responsible for the band gap in the spectrum of $r \neq 3n$ superstructures, is plotted for clusters of different sizes in Fig. 7. We see that for a generic

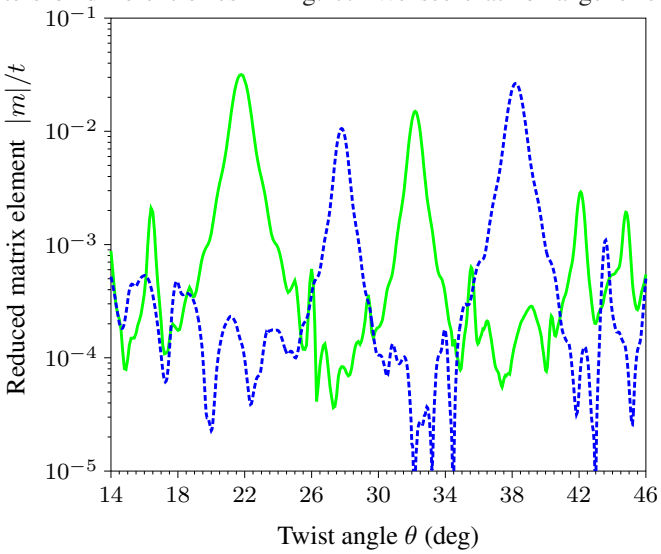

FIG. 6: The matrix element $|m|$ as a function of the twist angle θ. The radius of the cluster is $R = 60a_0$. The (green) solid curve shows the value of $|m|$ which is responsible for the opening of the band gap Δ in the structures with $r \neq 3n$, Figure 2(a). The (blue) dashed curve shows the matrix element inducing the band splitting in structures with $r = 3n$, Figure 2(b). The maxima of both curves are located at the angles $\theta_{(m_0,r)}$ corresponding to the superstructures with small r and m_0. For example, the strongest maxima of the (green) solid curve are at $\theta_{(1,1)} \approx 21.8^\circ$ and $\theta_{(1,2)} = 32.2^\circ$. For the (blue) dashed curve these are at $\theta_{(2,3)} = 27.8^\circ$ and $\theta_{(1,3)} = 38.2^\circ$. Note that $\theta_{(1,1)} + \theta_{(1,3)} = 60^\circ$ and $\theta_{(1,2)} + \theta_{(2,3)} = 60^\circ$, in agreement with Eq. (40).

value of the twist angle, the quantity $|m|$ quickly decreases with increasing R. At the same time, when θ corresponds to commensurate superlattices with small supercell size, $|m|$ remains constant ($\theta \approx 16.7^\circ, 21.8^\circ$). For somewhat larger supercell sizes ($\theta = 25.0^\circ, 26.0^\circ, 29.4^\circ$) the band splitting initially decreases, only to saturate at larger radii. The stabilization occurs when R sufficiently exceeds the supercell size. As an example, consider the $\theta = 26.0^\circ$ and $\theta = 29.4^\circ$ twist angles. In both cases, the matrix element stops changing when $R \geq 60a_0$. To weaken the edge effects for a finite cluster, our numerical procedure (see Appendix for details) confines the electron wave function within the effective radius $R_{\rm eff} < R$, defined as

$$R_{\rm eff} \approx R/2.2. \tag{41}$$

A physical cluster radius of $60a_0$ corresponds to the effective radius $R_{\rm eff} \approx 27a_0$. The latter number is comparable to the supercell size of $15a_0$ and $16a_0$ for such values of θ. If $\theta = 25.0^\circ$, the growth of $|m|$ is stabilized at $R = 90a_0$, or $R_{\rm eff} = 41a_0$. This is of the order of $L_{\rm sc} = 20a_0$ for the $\theta = 25.0^\circ$ superstructure. We see that for these three angles the matrix element saturates when $R_{\rm eff} \gtrsim 2L_{\rm sc}$.

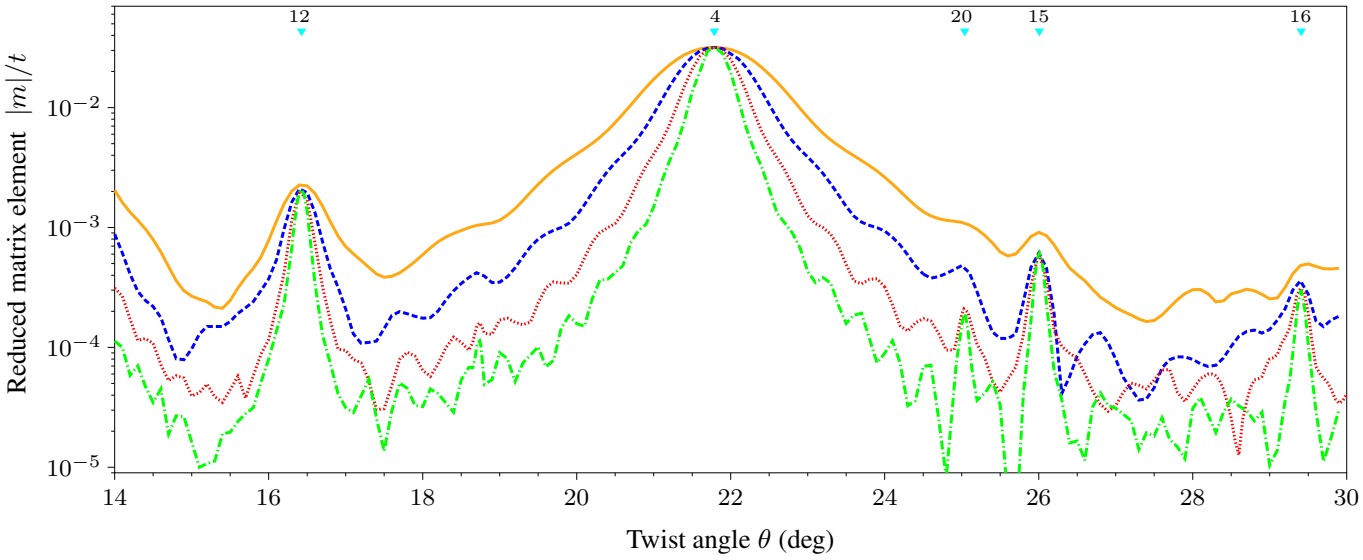

FIG. 7: The matrix element $|m|$ as a function of the twist angle for clusters of different radii. Four curves in this figure correspond to the following values of the effective cluster radius (for details, see Appendix): $R = 40a_0$ is shown by the solid (yellow) curve on top, $R = 60a_0$ by the dashed (blue) curve, $R = 90a_0$ by the dotted (red) curve, and $R = 130a_0$ is shown by the dash-dotted (green) curve at the bottom. The triangles at the top edge of the figure mark the commensurate angles with relatively small supercell linear size ($L_{\rm sc} \leq 20a_0$). The numbers above these triangles show the number of graphene's unit cells inside the supercell ($N/4$). One can notice that, at sufficiently large values of R, a peak forms at every marked angle.

The curves shown in Fig. 7 demonstrate that for finite clusters the matrix elements responsible for the gap are smooth functions of θ, unlike the data for infinite systems shown in Fig. 3. However, the results presented in Fig. 7 should not be interpreted as the dependence of the band gap versus the twist angle. As condition (31) implies, to decide if the tBLG spectrum has a gap (more precisely, pseudogap), it is necessary to compare $|m|$ against the dimensional quantization energy

$$\delta\varepsilon \sim \frac{v_{\rm F}}{R}\,. \tag{42}$$

Equivalently, the scale $v_{\rm F}/|m|$ should be smaller than R.

To describe the crossover between gapless and gapped regimes, let us analyze Fig. 8, where we replotted the data presented in Fig. 7 in a new manner: for a given curve, the angle θ is fixed, while the cluster size varies. The range of the twist angles in Fig. 8 is restricted to the vicinity of $\theta_0 \approx 21.8°$. We consider here only the angles $\theta < \theta_0$, since for $\theta > \theta_0$ the results are almost symmetric. The angle θ_0 corresponds to the smallest supercell possible for a tBLG. At $\theta = \theta_0$, the value of $|m|$ is the largest, see Fig. 6.

Panel (a) of Fig. 8 shows $|m(R)|$ as an implicit function of the dimensional quantization energy $\delta\varepsilon(R)$. In panel (b) the length scale $v_{\rm F}/|m|$ is plotted as a function of R. In both panels of Fig. 8 the dash-dotted straight lines are set by the equation $|m| = \delta\varepsilon$. These lines mark the crossover from the gapless ($|m| < \delta\varepsilon$) to the gapped ($|m| > \delta\varepsilon$) regimes.

The crossover can occur when the size of the cluster becomes sufficiently large. For example, if the twist angle is exactly commensurate (solid green curves on both panels), the increase of R, and concomitant decrease of $\delta\varepsilon$, pushes the sample from a gapless state to a state with single-electron gap. The data presented suggest that the crossover occurs when $R \approx 50a_0$, or, equivalently, $R_{\rm eff} \approx 23a_0$.

If deviations from the commensurate angle is small ($\theta \approx 22.0°$, dashed blue curve) the situation remains qualitatively the same: the gapless regime at small R is replaced by a gapped regime at larger R. For stronger deviations (e.g., $\theta \approx 22.4°$, dash-dotted orange curve) the system never leaves the gapless regime for any R. When $\theta = \theta^* \approx 22.2°$, the corresponding curve touches the crossover line. The angle θ^* separates two types of behavior. If $\theta > \theta^*$, the system is gapless even when the cluster is large. When $\theta_0 < \theta < \theta^*$, the crossover to the gapped regime can occur with increasing R. This analysis demonstrates that, to observe the single-electron gap caused by the interlayer tunneling near the commensurate angle $21.8°$, the twist must be controlled with an accuracy $\delta\theta \approx |\theta^* - \theta_0| \approx 0.4°$.

The same procedure can be performed near another "good" angle $\theta \approx 32.2°$, corresponding to $r = 2$ and $m_0 = 1$, see Fig. 6. The matrix element for this superstructure is roughly two times smaller than that for the structure with $r = m_0 = 1$ ($\theta \approx 21.8°$). Consequently, the radius of the clusters must be doubled to have a chance to be in the gapped regime. The increase in R translates into a more stringent requirement on the fine-tuning of θ: to observe the gap, the deviation from the commensurate angle must satisfy $\delta\theta \sim 0.1°$. Such a decrease in the allowed deviation of $\delta\theta$ can be understood as follows. A smaller $|m|$ implies that a larger R is necessary to enter the gapped regime. However, for larger clusters the maxima in Fig. 7 become sharper; consequently, the matrix element becomes very sensitive to the value of the twist angle. Therefore,

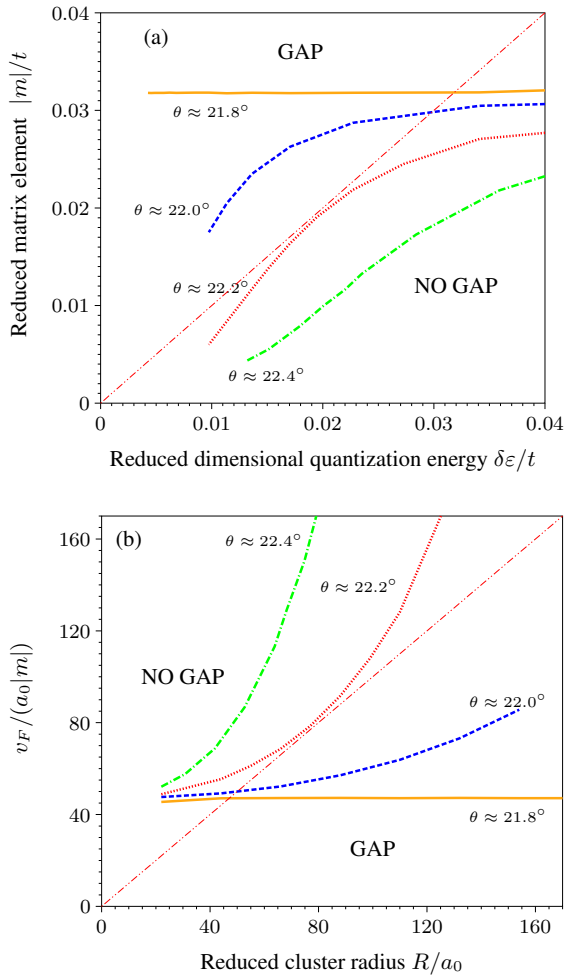

FIG. 8: Crossover between the gapless and gapped regimes. Panel (a) shows the parametric plots of the matrix element $|m(R)|$ versus the dimensional quantization energy $\delta\varepsilon(R)$ for several values of θ. The twist angle θ is constrained to the vicinity of the "good" commensurate angle $\theta_0 \approx 21.8^\circ$. The thin dash-dotted (red) straight line is determined by the equation $|m| = \delta\varepsilon$, marking the crossover between gapless ($|m| < \delta\varepsilon$) and gapped ($|m| > \delta\varepsilon$) spectra. Exactly at the commensurate angle [solid (yellow) curve] the system is gapless at larger $\delta\varepsilon$ (smaller R). It enters into a gapped regime for larger cluster size (smaller $\delta\varepsilon$). The [dashed (blue)] curve for 22.0° demonstrates similar behavior. When deviation from the "good" angle is higher [e.g., $\theta \approx 22.4^\circ$, dash-dotted (green) curve] the system never enters into the gapped regime. The angle $\theta^* \approx 22.2^\circ$ separates two types of behavior [and the corresponding dotted (red) curve touches the line $|m| = \delta\varepsilon$ when $\delta\varepsilon \approx 0.015t$]. In panel (b) the same data are plotted in a different manner: instead of comparing the dimensional quantization energy and $|m|$, panel (b) allows us to compare the cluster radius R and the length scale $v_\mathrm{F}/|m|$. The results for $\theta < 21.8^\circ$ are almost symmetric.

even a weak deviation from the "good" angle may push $|m|$ below $\delta\varepsilon$.

Investigations of superstructures with larger supercells place heavy requirements on computational resources. Indeed, large supercells correspond to exponentially small matrix elements, which means that exponentially large cluster sizes must be studied to enter the regime $\delta\varepsilon > |m|$. Such studies are computationally impractical. Thus, we must rely on the information collected above to draw conclusions.

VI. DISCUSSION AND CONCLUSIONS

The single-electron gap in the tBLG spectrum is a particularly challenging and interesting property. This gap demonstrates "fractal" oscillations when changing the twist angle (shown in Fig. 6), unlike, for example, the Fermi velocity, which varies smoothly. These oscillations are an artifact of the assumption that an electron propagates inside a perfect infinite tBLG lattice. In a realistic situation, the coherent propagation of a wave packet through the lattice is limited by the finiteness of the sample size L, and/or disorder scattering.

A particular example of disorder, one-dimensional wrinkles, was considered in Sec. IV. Defects of this kind are of interest due to two main reasons. First, it is an inherent type of disorder in graphene systems. Second, a linear defect is an effective source of scattering for low-energy Dirac quasiparticles, which is of importance for tBLG, with its flat bands and low-energy Van Hove singularity. Let us also comment that, since one-dimensional defects are very effective in destroying coherence, the fragile phenomenology of the marginal Fermi liquid, predicted for undoped graphene[36–38], may not survive in a sample with a sufficient concentration of wrinkles.

When the coherent propagation length $l_\mathrm{coh} = \min\{l_\mathrm{m}, L\}$ is finite, the diffraction effects associated with the superstructures with large supercells are destroyed. As a result, small gaps corresponding to such superlattices disappear. The stronger gaps can become observable, provided that (a) the length l_coh is sufficiently large, and (b) the deviation of the twist angle from a "good" value is sufficiently small.

The condition (a) is very general. It is necessary to remember that the band splitting Δ_s and, consequently, the gap is washed away by the disorder, or masked by finite size quantization, if $\Delta_s < v_\mathrm{F}/l_\mathrm{coh}$. This implies that the gap, or pseudogap, may be observed only when $l_\mathrm{coh} \gg v_\mathrm{F}/\Delta_s$.

Regarding condition (b), we have seen that the matrix element responsible for the opening of the gap is very sensitive to the shift $\delta\theta$ of the twist angle away from the "good" value. If θ coincides with a "good" angle ($\delta\theta = 0$), the matrix element becomes independent of l_coh for sufficiently large l_coh. Thus, exactly at a "good" angle the pseudogap or gap can be measured in a large sample of high purity. For small deviations from such an angle, the value of Δ_s decreases somewhat as l_coh grows, but the same qualitative picture endures.

However, as $\delta\theta$ departs from zero, the stabilization of the gap and the band splitting Δ_s at larger l_coh does not occur, see Fig. 8. Instead, the matrix element quickly collapses with increasing l_coh. As a result, for large deviations of θ from the "good" angle, the gapped regime never occurs.

Our analysis demonstrates that the experimental observation of the single-electron gap caused by the superlattice scattering is extremely unlikely, unless a very precise tuning of the twist angle to the "good" values is achieved. Such control may be enforced externally[39]. Alternatively, one can specu-

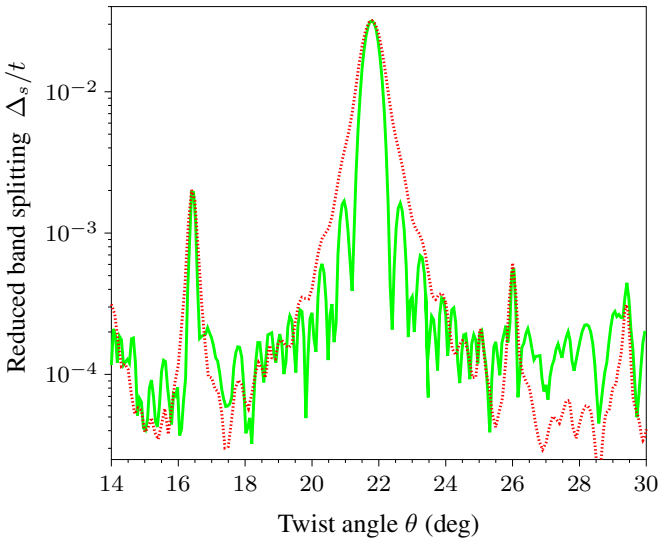

FIG. 9: Effect of the exponential decay of the wave function. The band splitting calculated for different values of ζ, see Eq. (A2). The $\zeta = 2.2$ data (dotted red curve) shows a smoother behavior than the $\zeta = 1.1$ data (solid green curve). The radius of the cluster is $90a_0$ for both curves.

late that commensurate angles correspond to local minima of the interlayer interaction potential. Consequently, the bilayer might spontaneously lock the twist angle to these angle values. However, such a possibility is, at this point, nothing but a hypothesis, and further research is required to support or refute it.

To conclude, we studied the dependence of the single-electron gap in finite clusters of tBLG. We demonstrated that the variation of the twist angle causes a crossover between gapless and gapped regimes, provided that the coherent propagation of an electron is limited by some finite length scale. Either the finiteness of the sample or the mean free path due to the disorder scattering may generate the latter length scale. To observe the gap experimentally it is necessary to have a sample of sufficient purity, and possess the ability to tune the twist angle accurately.

Appendix A: Details of numerical procedure

Here we briefly outline additional details of our numerical procedure which were too specialized to be included in the main text.

To calculate the matrix elements in Eq. (23) we use the following expression for the inter-layer hopping amplitude

$$t_\perp(\mathbf{r};\mathbf{r}') = \cos^2\alpha\; V_\sigma(\mathbf{r};\mathbf{r}') + \sin^2\alpha\; V_\pi(\mathbf{r};\mathbf{r}')\,,$$
$$\cos\alpha = \frac{d}{\sqrt{d^2+(\mathbf{r}-\mathbf{r}')^2}}\,, \qquad \text{(A1)}$$

where $d = 3.32\,\text{Å}$ is the interlayer distance, $\mathbf{r}$ and $\mathbf{r}'$ are 2D coordinates of the carbon atoms in the bottom and top layers, respectively, and V_σ and V_π are the 'Slater-Koster' functions, which we choose in the form of Eq. (1) of Ref. 33. In that paper the tunneling amplitude of an electron from one atom to another depends not only on the relative positions these two atoms, but also on the positions of other atoms in the crystal via the screening function S. The latter one has several fitting parameters, which we choose such that the function $t_\perp(\mathbf{r};\mathbf{r}')$ would correctly describe the first several interlayer hopping amplitudes of the AB bilayer ($\theta = 0$) graphene. More details can be found in Ref. 9.

It is known[40–43] that various types of localized states exist at the edges of graphene and graphene-based systems. Since we are interested in the bulk behavior, the influence of such states is to be reduced as much as possible. To decrease the effects of edge phenomena we introduced an exponential decay of the wave function from the cluster center toward the edges. Specifically, the matrix element Eq. (23) is calculated using the wave function for the layer 1

$$\psi_\gamma^{1\alpha}(\mathbf{r}_\mathbf{n}^{1\beta}) = \mathcal{N}\exp(-i\mathbf{K}_\gamma\mathbf{r}_\mathbf{n}^{1\alpha} - \zeta|\mathbf{r}_\mathbf{n}^{1\alpha}|/R)\delta_{\alpha\beta}\,, \qquad \text{(A2)}$$

where $\mathbf{K}_\gamma$ is the Dirac point corresponding to the chirality γ, $\delta_{\alpha\beta}$ is the Kronecker symbol, and $\zeta = 2.2$ is a numerical coefficient. In layer 2 the wave function is constructed in a similar manner. A wave function in layer 2 matches a wave function in layer 1 after an appropriate rotation. For finite samples, the wave functions are normalized to unity, with $\mathcal{N}$ being the normalization constant. It is worth noting that for infinite samples a different normalization condition should be used: $\sum_\mathbf{n}|\psi_\gamma^{i\alpha}(\mathbf{r}_\mathbf{n}^{i\alpha})|^2 = 1$, where the sum is taken over sites inside one supercell.

The magnitude of the wave function decreases away from the cluster center. The value of the numerical factor $\zeta = 2.2$ was chosen empirically. If ζ is too large, the effective size of the cluster

$$R_\text{eff} \sim R/\zeta \qquad \text{(A3)}$$

shrinks significantly below its nominal radius R; thus, we are forced to study computationally expensive cases of large R. If ζ is too small, the edge effects make the data very "noisy", see Fig. 9.

Interpreting our numerical data one must keep in mind that for finite R and arbitrary θ the absolute values of the non-zero elements of the matrix M, Eq. (24), may be slightly different from each other. However, we checked numerically that this disparity is not significant, at least for commensurate structures and larger clusters.

The data presented were collected for clusters in which the rotation axis passes through the geometrical center of the cluster. One can shift the rotation axis off the cluster center by the vector $\mathbf{T} = n\mathbf{a}_1 + m\mathbf{a}_2$, where n, m are integers. As long as $|\mathbf{T}| \ll R$, it is expected that the matrix M is independent of $\mathbf{T}$. We verified that this is indeed the case.

Acknowledgments.

This work was supported in part by RFBR (Grants Nos. 14-02-00276, 14-02-00058, 12-02-00339). F.N. was partially

supported by: the RIKEN iTHES Project, the MURI Center for Dynamic Magneto-Optics via the AFOSR Award No. FA9550-14-1-0040, the Japan Society for the Promotion of Science (KAKENHI), the ImPACT program of JST, CREST, and a grant from the John Templeton Foundation.

[1] A. Luican, G. Li, A. Reina, J. Kong, R. R. Nair, K. S. Novoselov, A. K. Geim, and E. Y. Andrei, "Single-Layer Behavior and Its Breakdown in Twisted Graphene Layers," Phys. Rev. Lett. **106**, 126802 (2011).

[2] L. Brown, R. Hovden, P. Huang, M. Wojcik, D. A. Muller, and J. Park, "Twinning and Twisting of Tri- and Bilayer Graphene," Nano Lett. **12**, 1609 (2012).

[3] I. Brihuega, P. Mallet, H. González-Herrero, G. Trambly de Laissardière, M. M. Ugeda, L. Magaud, J. M. Gómez-Rodríguez, F. Ynduráin, and J.-Y. Veuillen, "Unraveling the Intrinsic and Robust Nature of van Hove Singularities in Twisted Bilayer Graphene by Scanning Tunneling Microscopy and Theoretical Analysis," Phys. Rev. Lett. **109**, 196802 (2012).

[4] W. Yan, M. Liu, R.-F. Dou, L. Meng, L. Feng, Z.-D. Chu, Y. Zhang, Z. Liu, J.-C. Nie, and L. He, "Angle-Dependent van Hove Singularities in a Slightly Twisted Graphene Bilayer," Phys. Rev. Lett. **109**, 126801 (2012).

[5] Z. Ni, Y. Wang, T. Yu, Y. You, and Z. Shen, "Reduction of Fermi velocity in folded graphene observed by resonance Raman spectroscopy," Phys. Rev. B **77**, 235403 (2008).

[6] R. W. Havener, H. Zhuang, L. Brown, R. G. Hennig, and J. Park, "Angle-Resolved Raman Imaging of Interlayer Rotations and Interactions in Twisted Bilayer Graphene," Nano Lett. **12**, 3162 (2012).

[7] T. Ohta, J. T. Robinson, P. J. Feibelman, A. Bostwick, E. Rotenberg, and T. E. Beechem, "Evidence for Interlayer Coupling and Moiré Periodic Potentials in Twisted Bilayer Graphene," Phys. Rev. Lett. **109**, 186807 (2012).

[8] K. S. Kim, A. L. Walter, L. Moreschini, T. Seyller, K. Horn, E. Rotenberg, and A. Bostwick, "Coexisting massive and massless Dirac fermions in symmetry-broken bilayer graphene," Nat. Mater. **12**, 887 (2013).

[9] A. O. Sboychakov, A. L. Rakhmanov, A. V. Rozhkov, and F. Nori, "Electronic spectrum of twisted bilayer graphene," Phys. Rev. B **92**, 075402 (2015).

[10] D. Weckbecker, S. Shallcross, M. Fleischmann, N. Ray, S. Sharma, and O. Pankratov, "Low-energy theory for the graphene twist bilayer," Phys. Rev. B **93**, 035452 (2016).

[11] M.V. der Donck, C.D. Beule, B. Partoens, F.M. Peeters, and B.V. Duppen, 2D Materials **3**, 035015 (2016).

[12] D. S. Lee, C. Riedl, T. Beringer, A. H. Castro Neto, K. von Klitzing, U. Starke, and J. H. Smet, "Quantum Hall Effect in Twisted Bilayer Graphene," Phys. Rev. Lett. **107**, 216602 (2011).

[13] J. D. Sanchez-Yamagishi, T. Taychatanapat, K. Watanabe, T. Taniguchi, A. Yacoby, and P. Jarillo-Herrero, "Quantum Hall Effect, Screening, and Layer-Polarized Insulating States in Twisted Bilayer Graphene," Phys. Rev. Lett. **108**, 076601 (2012).

[14] J. Park, W. C. Mitchel, S. Elhamri, L. Grazulis, J. Hoelscher, K. Mahalingam, C. Hwang, S.-K. Mo, and J. Lee, "Observation of the intrinsic bandgap behaviour in as-grown epitaxial twisted graphene," Nat. Commun. **6**, 5677 (2015).

[15] A. Rozhkov, A. Sboychakov, A. Rakhmanov, and F. Nori, "Electronic properties of graphene-based bilayer systems," Phys. Rep. **648**, 1 (2016).

[16] K. Hermann, "Periodic overlayers and moiré patterns: theoretical studies of geometric properties", J. Phys.: Condens. Matter **24**, 314210 (2012).

[17] A. N. Kolmogorov and V. H. Crespi, "Registry-dependent interlayer potential for graphitic systems," Phys. Rev. B **71**, 235415 (2005).

[18] S. Latil, V. Meunier, and L. Henrard, "Massless fermions in multilayer graphitic systems with misoriented layers: *Ab initio* calculations and experimental fingerprints," Phys. Rev. B **76**, 201402 (2007).

[19] S. Shallcross, S. Sharma, and O. Pankratov, "Emergent momentum scale, localization, and van Hove singularities in the graphene twist bilayer," Phys. Rev. B **87**, 245403 (2013).

[20] S. Shallcross, S. Sharma, E. Kandelaki, and O. A. Pankratov, "Electronic structure of turbostratic graphene," Phys. Rev. B **81**, 165105 (2010).

[21] W. Landgraf, S. Shallcross, K. Türschmann, D. Weckbecker, and O. Pankratov, "Electronic structure of twisted graphene flakes," Phys. Rev. B **87**, 075433 (2013).

[22] S. Shallcross, S. Sharma, and O. A. Pankratov, "Quantum Interference at the Twist Boundary in Graphene," Phys. Rev. Lett. **101**, 056803 (2008).

[23] G. Trambly de Laissardière, D. Mayou, and L. Magaud, "Localization of Dirac Electrons in Rotated Graphene Bilayers," Nano Lett. **10**, 804 (2010).

[24] G. Trambly de Laissardière, D. Mayou, and L. Magaud, "Numerical studies of confined states in rotated bilayers of graphene," Phys. Rev. B **86**, 125413 (2012).

[25] E. Suárez Morell, J. D. Correa, P. Vargas, M. Pacheco, and Z. Barticevic, "Flat bands in slightly twisted bilayer graphene: Tight-binding calculations," Phys. Rev. B **82**, 121407 (2010).

[26] E. J. Mele, "Interlayer coupling in rotationally faulted multilayer graphenes," J. Phys. D: Appl. Phys. **45**, 154004 (2012).

[27] J. M. B. Lopes dos Santos, N. M. R. Peres, and A. H. Castro Neto, "Graphene Bilayer with a Twist: Electronic Structure," Phys. Rev. Lett. **99**, 256802 (2007).

[28] J. M. B. Lopes dos Santos, N. M. R. Peres, and A. H. Castro Neto, "Continuum model of the twisted graphene bilayer," Phys. Rev. B **86**, 155449 (2012).

[29] R. Bistritzer and A. H. MacDonald, "Moiré bands in twisted double-layer graphene," Proceedings of the National Academy of Sciences **108**, 12233 (2011).

[30] E. J. Mele, "Commensuration and interlayer coherence in twisted bilayer graphene," Phys. Rev. B **81**, 161405 (2010).

[31] E. J. Mele, "Band symmetries and singularities in twisted multilayer graphene," Phys. Rev. B **84**, 235439 (2011).

[32] P. San-Jose, J. González, and F. Guinea, "Non-Abelian Gauge Potentials in Graphene Bilayers," Phys. Rev. Lett. **108**, 216802 (2012).

[33] M. S. Tang, C. Z. Wang, C. T. Chan, and K. M. Ho, "Environment-dependent tight-binding potential model," Phys. Rev. B **53**, 979 (1996).

[34] A. Castro Neto, F. Guinea, N. Peres, K. Novoselov, and A. Geim, "The electronic properties of graphene," Rev. Mod. Phys. **81**, 109 (2009).

[35] V. M. Pereira, J. M. B. Lopes dos Santos, and A. H. Castro Neto, "Modeling disorder in graphene," Phys. Rev. B **77**, 115109 (2008).

[36] J. González, F. Guinea, and M. A. H. Vozmediano, "Unconventional Quasiparticle Lifetime in Graphite," Phys. Rev. Lett. **77**, 3589 (1996).
[37] S. Das Sarma, E. H. Hwang, and W.-K. Tse, "Many-body interaction effects in doped and undoped graphene: Fermi liquid versus non-Fermi liquid," Phys. Rev. B **75**, 121406 (2007).
[38] V. N. Kotov, B. Uchoa, V. M. Pereira, F. Guinea, and A. H. Castro Neto, "Electron-Electron Interactions in Graphene: Current Status and Perspectives," Rev. Mod. Phys. **84**, 1067 (2012).
[39] E. Koren, I. Leven, E. Lörtscher, A. Knoll, O. Hod, and U. Duerig, "Coherent commensurate electronic states at the interface between misoriented graphene layers," Nat. Nano. **11**, 752 (2016).
[40] K. Nakada, M. Fujita, G. Dresselhaus, and M. S. Dresselhaus, "Edge state in graphene ribbons: Nanometer size effect and edge shape dependence," Phys. Rev. B **54**, 17954 (1996).
[41] P. A. Maksimov, A. V. Rozhkov, and A. O. Sboychakov, "Localized electron states near the armchair edge of graphene," Phys. Rev. B **88**, 245421 (2013).
[42] I. V. Zagorodnev, Z. A. Devizorova, and V. V. Enaldiev, "Resonant electron scattering by a graphene antidot," Phys. Rev. B **92**, 195413 (2015).
[43] A. Rozhkov, G. Giavaras, Y. P. Bliokh, V. Freilikher, and F. Nori, "Electronic properties of mesoscopic graphene structures: Charge confinement and control of spin and charge transport," Phys. Rep. **503**, 77 (2011).